

Time-Resolved Focused Ion Beam Microscopy: Modeling, Estimation Methods, and Analyses

Minxu Peng, John Murray-Bruce, and Vivek K Goyal

Abstract—In a focused ion beam (FIB) microscope, source particles interact with a small volume of a sample to generate secondary electrons that are detected, pixel by pixel, to produce a micrograph. Randomness of the number of incident particles causes excess variation in the micrograph, beyond the variation in the underlying particle–sample interaction. We recently demonstrated that joint processing of multiple time-resolved measurements from a single pixel can mitigate this effect of source shot noise in helium ion microscopy. This paper is focused on establishing a rigorous framework for understanding the potential for this approach. It introduces idealized continuous- and discrete-time abstractions of FIB microscopy with direct electron detection and estimation-theoretic limits of imaging performance under these measurement models. Novel estimators for use with continuous-time measurements are introduced and analyzed, and estimators for use with discrete-time measurements are analyzed and shown to approach their continuous-time counterparts as time resolution is increased. Simulated FIB microscopy results are consistent with theoretical analyses and demonstrate that substantial improvements over conventional FIB microscopy image formation are made possible by time-resolved measurement.

Index Terms—computational imaging, Fisher information, gallium ion microscopy, helium ion microscopy, scanning electron microscopy, Poisson processes, shot noise, statistical modeling and estimation.

I. INTRODUCTION

THE ability to image the structure of a sample at nanoscale resolution using microscopes that scan samples with a focused beam of particles is critical in material science and the life sciences. In a scanning electron microscope (SEM) [1], a focused electron beam is raster scanned over the sample, causing the sample to emit secondary electrons (SEs). An SEM is capable of providing information regarding composition and distribution of sample components. Resembling an SEM, a focused ion beam (FIB) microscope [2] instead uses a focused beam of ions, such as gallium, helium, or xenon. As one member of the FIB microscope family, a helium ion microscope (HIM) [3] offers many advantages compared to an SEM, leading to widespread use in semiconductor and biological imaging [4]–[7]. The interaction volume with the sample is much smaller for ions compared to that for electrons, resulting in higher contrast [8]. Higher particle mass also

leads to higher overall SE yield [9], [10]. Furthermore, to image insulating samples with an SEM, prior deposition of a conductive coating is required to prevent the accumulation of electron charges on the sample; an HIM uses an electron flood gun to prevent charge accumulation, thus avoiding the masking of subtle features by a coating [11].

The number of incident ions determines the number of sample interactions that can be measured. Hence, increasing this number—through increased beam current or increased dwell time—will ideally create measurements that are more informative about the mean number of SEs per incident ion, which is the sample property of interest. However, the vastly greater mass of ions compared to electrons (by a factor of 7.3×10^3 for helium or 1.3×10^5 for gallium) makes sputtering much more significant for FIB microscopy than for SEM. Various studies have shown how the sputtering damage induced by helium ions evolves with increasing numbers of incident ions [12]–[14], and this damage is often determinative of the best possible image quality. Dose is conventionally defined as the number of incident ions per unit area, and dose limits to prevent significant damage have been measured for certain materials and imaging configurations. For example, a safe imaging dose for suspended graphene is as low as 10^{13} to 10^{14} per square centimeter [15]. It follows, for example, that a $(10 \text{ nm})^2$ pixel should be subjected to only 10 to 100 ions. In our abstractions, we dispense with spatial dimensions and hereafter express doses per pixel rather than per unit area; expressed per pixel, finer resolution necessitates lower dose limits. While randomized subsampling combined with regularized reconstruction can sometimes yield high-quality images from reduced doses [16]–[18], this requires piecewise smooth image structure. Here we restrict our attention to pixelwise acquisition and estimation methods that do not rely on such assumptions.

We recently introduced the concept of *time-resolved* (TR) measurements in FIB microscopy to mean dividing any given pixel dwell time t into n dwell times t/n for some integer $n > 1$ [19]. Without proofs, we gave theoretical evidence that a set of TR measurements is fundamentally more informative than a single measurement with the same total dose. Experiments with HIM data demonstrated mean-squared error (MSE) improvement by about a factor of 4 at doses of 1.0 and 2.5 incident ions per pixel. Importantly, this use of time resolution is entirely for the purpose of making the measurements more informative without increasing the total dose. It is not for imaging of dynamic samples and hence not comparable to any previous use of time resolution in microscopy.

The Zeiss ORION NanoFab HIM used in [19], like most

M. Peng and V. K. Goyal are with the Department of Electrical and Computer Engineering, Boston University, Boston, MA 02215 USA (e-mail: mxpeng@bu.edu; v.goyal@ieee.org).

J. Murray-Bruce is with the Department of Computer Science and Engineering, University of South Florida, Tampa, FL 33620 USA (e-mail: murraybruce@usf.edu).

This work was supported in part by the US National Science Foundation under Grant No. 1422034 and Grant No. 1815896.

commercial FIB microscopes, uses indirect electron detection with a scintillator and photomultiplier tube. Although not yet prevalent, direct electron detection offers higher signal-to-noise ratio (SNR) as it avoids the statistical noises brought by electron–photon conversion and additional readout noise [20]. For example, Yamada et al. [21] demonstrated that the SNR of direct electron detection is 2.5 times higher than that of indirect mode at low dose. Furthermore, direct electron detection technology has also been applied to imaging in transmission electron microscopy to improve resolution [22].

In this paper, we develop comprehensive theoretical results for FIB microscopy with time-resolved direct SE detection. Indirect detection introduces many sources of noise, including spatial nonuniformity in the scintillator response, nonideal light transport from the scintillator to the photomultiplier tube, and variations in pulses generated by the photomultiplier tube. Though these effects were empirically modeled in [19], including them here would make already lengthy expressions considerably more complicated and more difficult to interpret. Restricting attention to direct detection allows us to concentrate on the implications of TR sensing for mitigation of source shot noise, separated from the effects of detection noise. While some results presented here add rigor to statements in [19], we more importantly introduce a new continuous-time abstraction for FIB microscopy that yields to more elegant analyses while also representing the ultimate limit of this technology. In addition to maximum likelihood (ML) estimation, our study includes plug-in estimators for which we can complete analytical performance analyses and that are easily generalized to settings in which SE detection is indirect.

A. Main Contributions

- *A new continuous-time probabilistic model for FIB microscopy wherein the data at any one pixel are related to a marked Poisson process.* Conventional and continuous- and discrete-time time-resolved observation models are different functions of the marked Poisson process.
- *Fisher information analyses.* We show that, at any ion dose level, continuous-time time-resolved measurements have Fisher information matching an upper bound that conventional measurements meet only in a low-dose limit. For conventional measurements, asymptotic expressions presented without proof in [19] are proven here.
- *Estimator analyses.* Biases and variances of quotient-mode estimators in both the continuous- and discrete-time settings are derived. Convergence of the discrete-time estimator’s performance to the performance of the continuous-time estimator is proven.

B. Outline

We introduce our mathematical abstraction for the operation of a FIB microscope in Section II. This leads to four measurement models: an unimplementable oracle model, conventional measurement, and continuous- and discrete-time time-resolved measurement. The oracle and conventional cases are analyzed

TABLE I: List of symbols and acronyms

η	mean secondary electron yield
$\hat{\eta}_{\text{oracle}}$	oracle estimator (8)
$\hat{\eta}_{\text{baseline}}$	baseline estimator (14)
$\hat{\eta}_{\text{CTQM}}$	continuous-time quotient mode estimator (28)
$\hat{\eta}_{\text{CTLQM}}$	continuous-time Lambert quotient mode estimator (29)
$\hat{\eta}_{\text{CTML}}$	continuous-time maximum likelihood estimator (30)
$\hat{\eta}_{\text{DTQM}}$	discrete-time quotient mode estimator (40)
$\hat{\eta}_{\text{DTLQM}}$	discrete-time Lambert quotient mode estimator (41)
$\hat{\eta}_{\text{DTML}}$	discrete-time maximum likelihood estimator (42)
λ	ion dose per pixel
Λ	dose per unit time
ρ	$P(X_i > 0) = 1 - e^{-\eta}$
i	ion index
k	discrete time index
n	number of subacquisitions
p	$P(Y_k > 0) = 1 - \exp(-(\lambda/n)(1 - e^{-\eta}))$
t	dwel time
$\mathcal{I}_Z(\eta; \lambda)$	Fisher information about η in Z with λ available
L	number of subacquisitions with positive SEs
\tilde{L}	zero-truncated version of L
M	number of incident ions
\tilde{M}	number of incident ions yielding positive SEs
T_i	i th ion incidence time
\tilde{T}_i	incidence time of i th ion to yield positive SEs
X_i	SEs detected due to i th incident ion
\tilde{X}_i	SEs detected due to i th ion to yield positive SEs
Y	total detected SEs
Y_k	detected SEs in k th subacquisition
\tilde{Y}_k	positive SE counts in a subacquisition
CRB	Cramér–Rao bound
CTTR	continuous-time time-resolved (see observation (6))
DTTR	discrete-time time-resolved (see observation (7))
FI	Fisher information
LQM	Lambert quotient mode
ML	maximum likelihood
QM	quotient mode
SE	secondary electron
TR	time-resolved

within Section II. Section III develops the novel continuous-time case in detail. Measurement distributions are derived, three estimators are introduced and simulated, and the performance of a quotient-mode estimator is rigorously analyzed. Section IV develops the discrete-time case first introduced in [19] in detail. Three estimators are simulated, and the performance of the discrete-time quotient-mode estimator is rigorously analyzed. Convergences of Fisher information and quotient-mode estimator performance to their continuous-time counterparts are shown. Section V compares all the estimators in a simulated HIM experiment, demonstrating substantial improvement of the time-resolved methods over the conventional interpretation of the collected data. Section VI provides concluding comments on how mean SE yield influences the advantages of TR methods, the time resolution necessary to capitalize on these advantages, the roles of the various estimators, and generalizations to indirect SE detection.

Table I summarizes the variables, symbols, and acronyms used in the manuscript.

II. MEASUREMENT MODELS AND BASIC ANALYSES

A. Physical Abstractions

Throughout this paper, we model the incident ions at the sample to be imaged as a Poisson process with known rate Λ per unit time. Imaging proceeds by raster scanning with known

dwelt time t at each pixel. Hence, the number of ions M incident on a pixel is a Poisson random variable with known parameter $\lambda = \Lambda t$. Since pixel area is not relevant in our abstraction, we refer to λ as the dose. The interaction of the i th incident ion with the sample causes a number X_i of SEs to be detected. All of these SE counts are mutually independent Poisson random variables with parameter η , independent of the incident-ion Poisson process, and estimation of the mean SE yield η is the objective of the imaging experiment. Our analysis is for each pixel separately, so no pixel indexing is necessary.

Note that a somewhat high 1 pA beam current corresponds to a rate of 6.2×10^6 ions per second, or a mean ion interarrival time of 160 ns. The interaction between an incident ion and the sample and the subsequent detection of SEs occurs within a few femtoseconds [23]. With the SE detections happening so quickly, we abstract the SE detections caused by an incident ion to be simultaneous with the ion incidence. Thus, the model can be described as a marked Poisson process $\{(T_1, X_1), (T_2, X_2), \dots\}$, where (T_1, T_2, \dots) is the arrival time sequence of the ions. The ion count M is the largest i such that $T_i \leq t$ (with $M = 0$ when $T_1 > t$). One realization on an interval $[0, t]$ is illustrated in Fig. 1(a). Note that the arrival times (horizontal) are arbitrary positive real numbers and the marks (vertical) are nonnegative integers.

Since cases of $X_i = 0$ produce no detected SEs, the corresponding ion arrival time is not observable in practice. Thus consider also the thinned process $\{(\tilde{T}_1, \tilde{X}_1), (\tilde{T}_2, \tilde{X}_2), \dots\}$, where \tilde{T}_i is the arrival time of the i th ion that produces a *positive* number of detected SEs and \tilde{X}_i is the corresponding number of detected SEs. Define \tilde{M} to be the largest i such that $\tilde{T}_i \leq t$ (with $\tilde{M} = 0$ when $\tilde{T}_1 > t$). Note that the thinned process is also a marked Poisson process because the events of the form $\{X_i = 0\}$, which determine whether an arrival in the original Poisson process is retained, are independent of the arrival time process. Fig. 1(b) illustrates the thinned process for the realization of the underlying process in Fig. 1(a).

Now suppose the observation time interval $[0, t]$ is evenly divided into n subintervals of length t/n . Counting the total number of SEs detected in each subinterval produces a discrete-time, discrete-valued random process:

$$Y_k = \sum_{\{i : T_i \in [(k-1)t/n, kt/n]\}} X_i, \quad k = 1, 2, \dots, n. \quad (1)$$

We call an observation over a subinterval a *subacquisition*. Fig. 1(c) illustrates the partition of $[0, t]$ into subintervals and Fig. 1(d) illustrates the resulting discrete-time process for the realization of the underlying process in Fig. 1(a). Because of the independence of a Poisson process over disjoint intervals, $\{Y_k\}_{k=1}^n$ is an independent and identically distributed (i.i.d.) process. We can also view $\{Y_k\}_{k=1}^n$ as a marked Bernoulli process, where $\{Y_k > 0\}$ indicates an arrival in discrete time slot k and the “mark” is then the (nonzero) value Y_k .

The abstraction described here applies similarly to SEM and FIB microscopy. The main difference is the typical values of the mean SE yield η . In SEM, neglecting topographical effects (which tend to increase yield), for a sample with atomic number up to 83, the SE yield at the maximizing electron

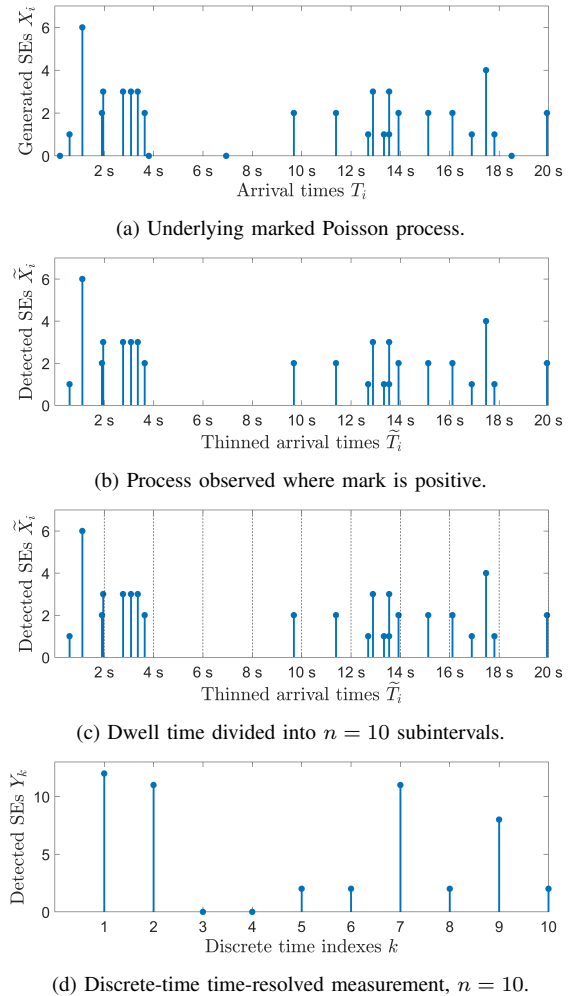


Fig. 1: Illustration of the random processes generated in the abstraction of FIB microscopy through one possible realization. (a) The underlying marked Poisson process $\{(T_1, X_1), (T_2, X_2), \dots\}$, with ion incident at times T_1, T_2, \dots generating detected SE counts X_1, X_2, \dots . (b) The marked Poisson process $\{(\tilde{T}_1, \tilde{X}_1), (\tilde{T}_2, \tilde{X}_2), \dots\}$, produced by discarding the ions for which no SEs are detected. (c) Illustration of dividing dwell time of $t = 20$ s into $n = 10$ subintervals of equal length. (d) The resulting discrete-time SE count process.

energy is typically 0.6 to 2 [24]. In FIB microscopy, SE yield is typically between 1 and 8 [25]. The advantages of TR measurements that are established in this paper diminish at smaller η values. Furthermore, in FIB microscopy, sample damage is more of an impediment to improving image quality by increasing dose [12]–[14]. Thus, we concentrate on FIB microscopy.

B. Measurement Models

We consider four measurement models for the probabilistic experiment described in Section II-A:

- *Oracle*: Observe

$$\{M, (T_1, X_1), (T_2, X_2), \dots, (T_M, X_M)\}. \quad (2)$$

Though no current instrument provides this information, this measurement model provides a useful benchmark.

- *Conventional*: Observe only

$$Y = \sum_{i=1}^M X_i. \quad (3)$$

This would be the standard operation of a FIB microscope that has direct detection of SEs. Note that

$$Y = \sum_{i=1}^{\tilde{M}} \tilde{X}_i \quad (4)$$

and

$$Y = \sum_{k=1}^n Y_k \quad (5)$$

are equivalent to the definition of Y . As the sum of a Poisson(λ) number of mutually independent Poisson(η) random variables, (3) is the simplest of the expressions.

- *Continuous-time time-resolved (CTTR)*: Observe

$$\{\tilde{M}, (\tilde{T}_1, \tilde{X}_1), (\tilde{T}_2, \tilde{X}_2), \dots, (\tilde{T}_{\tilde{M}}, \tilde{X}_{\tilde{M}})\}. \quad (6)$$

This is an idealization of a FIB microscope with direct detection of SEs with perfect temporal precision.

- *Discrete-time time-resolved (DTTR)*: Observe

$$\{Y_1, Y_2, \dots, Y_n\}. \quad (7)$$

This is a model for the use of a FIB microscope to collect a set of low-dose subacquisitions.

Having established these abstractions, we can reiterate that our principal goal is to demonstrate substantial improvements from time-resolved measurements. In our previous work [19], we introduced the concept of DTTR measurement along with estimators to apply with these measurements, and we showed empirical improvements over the trivial estimator that is routinely applied with conventional measurements. The analysis of estimators in that work is limited, and certain theoretical assertions are made without proofs. The CTTR model introduced here is easier to analyze and represents a bound for what can be done with DTTR measurements. We also provide new analyses of estimators for the DTTR model. Through these results and Monte Carlo simulations, the convergence of DTTR estimators to CTTR estimators as $n \rightarrow \infty$ can be understood precisely (see Sections IV-B and IV-D).

C. Analyses for Oracle Measurement

We initially assume $M = m > 0$. Then the oracle measurement (2) includes nonempty sets of ion arrival times $\{T_1, T_2, \dots, T_m\}$ and of SE counts $\{X_1, X_2, \dots, X_m\}$. The arrival times have beta distributions, with no dependence on parameter of interest η . Thus, arrival times are immaterial to estimation of η (i.e., redundant with knowing M). The SE counts are i.i.d. observations with the Poisson(η) distribution, and it is elementary to show that $Y = X_1 + X_2 + \dots + X_m$ is a sufficient statistic and that Y/m is an efficient estimator of η from the available data. In the case of $M = 0$, there is no basis for any estimate of η , so we must assign some arbitrarily chosen number η_0 .

From the arguments above, we define the oracle estimator

$$\hat{\eta}_{\text{oracle}}(M, X_1, X_2, \dots, X_M) = \begin{cases} \eta_0, & M = 0; \\ Y/M, & M > 0. \end{cases} \quad (8)$$

Conditioned on $M = m > 0$, the mean-squared error (MSE) of this estimator is η/m because Y has mean $m\eta$ and variance $m\eta$. Using the Poisson distribution for M and the total expectation theorem,

$$\text{MSE}(\hat{\eta}_{\text{oracle}}) = e^{-\lambda}(\eta - \eta_0)^2 + \sum_{m=1}^{\infty} \frac{\eta}{m} \frac{\lambda^m}{m!} e^{-\lambda}. \quad (9)$$

For large enough λ , the arbitrary guess of η_0 when $M = 0$ has little impact on the MSE. Approximating the second term using (60) from Appendix A gives

$$\text{MSE}(\hat{\eta}_{\text{oracle}}) \approx \frac{\eta}{\lambda} \quad \text{for large } \lambda. \quad (10)$$

D. Analyses for Conventional Measurement

It is straightforward to show that the conventional measurement Y has *Neyman Type A* probability mass function (PMF)

$$P_Y(y; \eta, \lambda) = \frac{e^{-\lambda} \eta^y}{y!} \sum_{m=0}^{\infty} \frac{(\lambda e^{-\eta})^m m^y}{m!}, \quad y = 0, 1, \dots, \quad (11)$$

mean

$$E[Y] = \lambda\eta, \quad (12)$$

and variance

$$\text{var}(Y) = \lambda\eta + \lambda\eta^2. \quad (13)$$

Starting from (3), (11) follows from the law of total probability, (12) from iterated expectation with conditioning on M , and (13) from the law of total variance with conditioning on M [19]. Reaching the same conclusions starting from (4) or (5) involves more complicated computations.

From (12), the baseline estimator

$$\hat{\eta}_{\text{baseline}}(Y) = \frac{Y}{\lambda} \quad (14)$$

is unbiased, and from (13) its MSE is

$$\text{MSE}(\hat{\eta}_{\text{baseline}}) = \frac{\eta(1 + \eta)}{\lambda}. \quad (15)$$

If λ ions were deterministically incident upon the sample, Y would be a Poisson($\lambda\eta$) random variable, with variance $\lambda\eta$, and the MSE of the baseline estimator would be η/λ . The excess variance in (13), consistent with experimental observations [26], and excess MSE in (15) are due to the random variation in the number of incident ions or the *source shot noise*. Our line of work mitigates this noise.

Since estimation under a Neyman Type A observation model is not well known, the potential efficiency of the baseline estimator is not evident. To this end, it is natural to evaluate the Fisher information (FI) about η in Y with λ as a known parameter, which we denote by $\mathcal{I}_Y(\eta; \lambda)$.

The FI is defined as

$$\mathcal{I}_Y(\eta; \lambda) = E \left[\left(\frac{\partial \log P_Y(y; \eta, \lambda)}{\partial \eta} \right)^2 ; \eta \right], \quad (16)$$

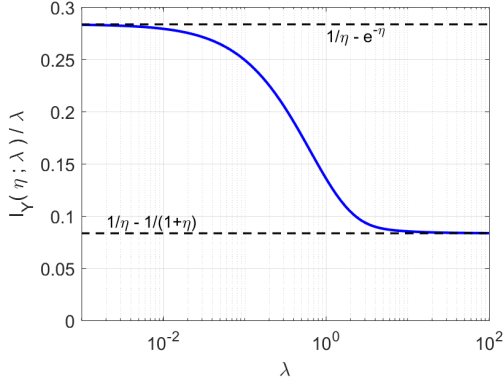


Fig. 2: Normalized Fisher information $\mathcal{I}_Y(\eta; \lambda)/\lambda$ as a function of λ for $\eta = 3$. The marked asymptotes are derived in Appendix B.

where a known non-random parameter in the expectation is emphasized by putting it after a semicolon. From (11),

$$\begin{aligned} \log P_Y(y; \eta, \lambda) &= -\lambda + y \log \eta - \log y! + \log \left(\sum_{m=0}^{\infty} \frac{(\lambda e^{-\eta})^m m^y}{m!} \right). \end{aligned}$$

Then taking the derivative with respect to η , we find that

$$\begin{aligned} \frac{\partial \log P_Y(y; \eta, \lambda)}{\partial \eta} &= \frac{y}{\eta} - \frac{\sum_{m=0}^{\infty} \frac{m(\lambda e^{-\eta})^m m^y}{m!}}{\sum_{m=0}^{\infty} \frac{(\lambda e^{-\eta})^m m^y}{m!}} \\ &\stackrel{(a)}{=} \frac{y}{\eta} - \frac{P_Y(y+1; \eta, \lambda) \frac{e^{-\lambda} \eta^{y+1}}{(y+1)!}}{P_Y(y; \eta, \lambda) \frac{e^{-\lambda} \eta^y}{y!}} \\ &= \frac{y}{\eta} - \frac{P_Y(y+1; \eta, \lambda) y + 1}{P_Y(y; \eta, \lambda) \eta}, \end{aligned}$$

where (a) follows from (11). The FI is the second moment of the above expression:

$$\mathcal{I}_Y(\eta; \lambda) = \sum_{y=0}^{\infty} \left(\frac{y}{\eta} - \frac{P_Y(y+1; \eta, \lambda) y + 1}{P_Y(y; \eta, \lambda) \eta} \right)^2 P_Y(y; \eta, \lambda). \quad (17)$$

While (17) is not readily comprehensible, it can be used to numerically evaluate $\mathcal{I}_Y(\eta; \lambda)$ and to derive certain useful asymptotic approximations and limits. One can interpret the ratio $\mathcal{I}_Y(\eta; \lambda)/\lambda$ as the information gain per incident ion. As illustrated in Fig. 2, this *normalized Fisher information* is a decreasing function of λ , with

$$\lim_{\lambda \rightarrow 0} \frac{\mathcal{I}_Y(\eta; \lambda)}{\lambda} = \frac{1}{\eta} - e^{-\eta} \quad (18)$$

and

$$\lim_{\lambda \rightarrow \infty} \frac{\mathcal{I}_Y(\eta; \lambda)}{\lambda} = \frac{1}{\eta(1+\eta)} = \frac{1}{\eta} - \frac{1}{1+\eta}. \quad (19)$$

Detailed derivations are provided in Appendix B.

Using (19) to write

$$\mathcal{I}_Y(\eta; \lambda) \approx \frac{\lambda}{\eta(1+\eta)} \quad \text{for large } \lambda, \quad (20)$$

we have a match to the reciprocal of the MSE in (15). Thus, the baseline estimator achieves the Cramér–Rao bound (CRB) asymptotically as $\lambda \rightarrow \infty$, but not otherwise (since the normalized FI is a decreasing function of λ).

One could seek improved estimators for low λ or improved lower bounds to demonstrate that substantially better estimators do not exist. We do not pursue those goals here. In practice, improved estimators for low λ may be of limited interest—even if they improve significantly upon the baseline estimator. For example, with reference to Fig. 2, FI suggests that one may be able to improve upon the baseline estimator by a factor of 3 at dose $\lambda = 10^{-2}$. However, even the lowest possible MSE would be quite high at such a low dose.

The key observation from Fig. 2 and the limits in (18) and (19) is that low-dose measurements are more informative per incident ion than high-dose measurements. The remainder of the paper studies methods to realize improvements related to this gap while operating at any dose level—not only low dose. Furthermore, notice that the MSE in (15) has a simple inversely proportional relationship with λ . Most performance bounds and empirical performances in this paper share this simple $1/\lambda$ behavior, so we place little emphasis on the performance as λ is varied. Instead, we concentrate on comparisons among different methods and the performance dependence on η .

III. CONTINUOUS-TIME TIME-RESOLVED MEASUREMENT

A. Measurement Distributions

The CTTR measurement (6) contains the number of incident ions that result in positive detected SEs \tilde{M} , the arrival times of these ions $\{\tilde{T}_1, \tilde{T}_2, \dots, \tilde{T}_{\tilde{M}}\}$, and the corresponding SE counts $\{\tilde{X}_1, \tilde{X}_2, \dots, \tilde{X}_{\tilde{M}}\}$. As noted in Section II-A, the mutual independence of the arrival times in the underlying process $\{T_1, T_2, \dots\}$ and all events of the form $\{X_i = 0\}$ cause the Poisson process property to be preserved.

Since $P(X_i = 0) = e^{-\eta}$, the rate Λ of the underlying process is reduced to $\Lambda(1 - e^{-\eta})$ for the thinned process. For the thinned ion count over dwell time t , we have $\tilde{M} \sim \text{Poisson}(\lambda(1 - e^{-\eta}))$, or more explicitly the PMF

$$P_{\tilde{M}}(\tilde{m}; \eta, \lambda) = \exp(-\lambda(1 - e^{-\eta})) \frac{(\lambda(1 - e^{-\eta}))^{\tilde{m}}}{\tilde{m}!}, \quad (21)$$

for $\tilde{m} = 0, 1, \dots$

The distribution of the \tilde{X}_i variables is simply the zero-truncation of the Poisson(η) distribution:

$$P_{\tilde{X}_i}(j; \eta) = \frac{e^{-\eta}}{1 - e^{-\eta}} \cdot \frac{\eta^j}{j!}, \quad j = 1, 2, \dots \quad (22)$$

While the interarrival times of the thinned process have a simple exponential distribution, this is not relevant to our estimation tasks: Under the CTTR measurement model, we have \tilde{M} available, and conditioned on \tilde{M} , the thinned arrival times have beta distributions with no dependence on the parameter of interest η .

B. Fisher Information

We would like to evaluate the FI about η in the CTTR measurement (6) with λ as a known parameter:

$$\begin{aligned} \mathcal{I}_{\text{CTTR}}(\eta; \lambda) &\stackrel{(a)}{=} \mathcal{I}_{(\tilde{T}_1, \tilde{X}_1), \dots, (\tilde{T}_M, \tilde{X}_M) | \tilde{M}}(\eta; \lambda) + \mathcal{I}_{\tilde{M}}(\eta; \lambda) \\ &\stackrel{(b)}{=} \mathcal{I}_{\tilde{X}_1, \dots, \tilde{X}_M | \tilde{M}}(\eta; \lambda) + \mathcal{I}_{\tilde{M}}(\eta; \lambda) \\ &\stackrel{(c)}{=} \mathbb{E} \left[\tilde{M} \right] \mathcal{I}_{\tilde{X}_i}(\eta; \lambda) + \mathcal{I}_{\tilde{M}}(\eta; \lambda) \\ &\stackrel{(d)}{=} \lambda(1 - e^{-\eta}) \mathcal{I}_{\tilde{X}_i}(\eta; \lambda) + \mathcal{I}_{\tilde{M}}(\eta; \lambda), \end{aligned} \quad (23)$$

where (a) follows from the chain rule for FI [27]; (b) from the conditional distribution of each \tilde{T}_i given \tilde{M} having no dependence on η ; (c) from additivity of FI and the independence of $\{\tilde{M}, \tilde{X}_1, \tilde{X}_2, \dots, \tilde{X}_M\}$; and (d) from substitution of the mean of \tilde{M} . Thus, we need to evaluate $\mathcal{I}_{\tilde{X}_i}(\eta; \lambda)$ and $\mathcal{I}_{\tilde{M}}(\eta; \lambda)$. The former, which represents the FI for estimating η from \tilde{X}_i is

$$\begin{aligned} \mathcal{I}_{\tilde{X}_i}(\eta; \lambda) &= \mathbb{E} \left[\left(\frac{\partial \log P_{\tilde{X}_i}(\tilde{X}_i; \eta, \lambda)}{\partial \eta} \right)^2 ; \eta \right] \\ &\stackrel{(a)}{=} \sum_{j=1}^{\infty} \left(\frac{j}{\eta} - \frac{1}{1 - e^{-\eta}} \right)^2 \frac{e^{-\eta}}{1 - e^{-\eta}} \frac{\eta^j}{j!} \\ &= \frac{1}{1 - e^{-\eta}} \frac{\eta + 1}{\eta} - \frac{1}{(1 - e^{-\eta})^2}, \end{aligned} \quad (24)$$

where (a) uses the PMF in (22). Similarly, $\mathcal{I}_{\tilde{M}}(\eta; \lambda)$, which represents the FI for estimating η from \tilde{M} , is

$$\begin{aligned} \mathcal{I}_{\tilde{M}}(\eta; \lambda) &= \mathbb{E} \left[\left(\frac{\partial \log P_{\tilde{M}}(\tilde{M}; \eta, \lambda)}{\partial \eta} \right)^2 ; \eta \right] \\ &\stackrel{(a)}{=} \sum_{j=0}^{\infty} \left(\frac{e^{-\eta}}{1 - e^{-\eta}} j - \lambda e^{-\eta} \right)^2 \frac{e^{-\lambda(1 - e^{-\eta})} [\lambda(1 - e^{-\eta})]^j}{j!} \\ &= \frac{\lambda e^{-\eta}}{e^{\eta} - 1}, \end{aligned} \quad (25)$$

where (a) uses the PMF in (21). Finally, substituting (24) and (25) into (23) gives

$$\mathcal{I}_{\text{CTTR}}(\eta; \lambda) = \lambda \left(\frac{1}{\eta} - e^{-\eta} \right). \quad (26)$$

Notice that the FI for CTTR measurement matches the low-dose asymptote given in (18). It is exact and holds for all values of λ . The greater FI for CTTR measurement than for conventional measurement is suggestive of being able to improve upon the baseline estimator (14). In the following sections, we define new estimators and demonstrate their improvements.

C. Estimators

In this section, we introduce estimators applicable to CTTR measurement (6). From (4), it is clear that the total number of detected SEs Y is available. As we have explained in the derivation of $\mathcal{I}_{\text{CTTR}}(\eta; \lambda)$ in Section III-B, with \tilde{M} available, there is no additional information about η in the

thinned ion incidence times $\{\tilde{T}_1, \tilde{T}_2, \dots, \tilde{T}_M\}$. Furthermore, with Y and \tilde{M} available, there is no additional information about η in the positive SE counts $\{\tilde{X}_1, \tilde{X}_2, \dots, \tilde{X}_M\}$. To see this, consider any observation vector $(\tilde{X}_1, \tilde{X}_2, \dots, \tilde{X}_M) = (j_1, j_2, \dots, j_m)$ conditioned on $\tilde{M} = \tilde{m}$. Using independence and (22), the likelihood of the observation (conditioned on $\tilde{M} = \tilde{m}$) is

$$\prod_{i=1}^{\tilde{m}} P_{\tilde{X}_i}(j_i; \eta) = \left(\frac{e^{-\eta}}{1 - e^{-\eta}} \right)^{\tilde{m}} \frac{\eta^{j_1 + j_2 + \dots + j_{\tilde{m}}}}{j_1! j_2! \dots j_{\tilde{m}}!}. \quad (27)$$

As a function of η , the dependence on SE counts is only through their sum. Hence, all the estimators in the section depend only on Y and \tilde{M} .

1) *Continuous-Time Quotient Mode Estimator*: Recall that the oracle estimator (8) divides the total SE count Y by the number of incident ions M . Using \tilde{M} as a proxy for the number of incident ions yields the *continuous-time quotient mode* (CTQM) estimator

$$\hat{\eta}_{\text{CTQM}}(\tilde{M}, Y) = \begin{cases} 0, & \tilde{M} = 0; \\ Y/\tilde{M}, & \tilde{M} > 0. \end{cases} \quad (28)$$

Note that the 0 estimate for $\tilde{M} = 0$ is not arbitrary, it is the ML estimate of η for this case. The name ‘‘quotient mode’’ is to acknowledge a similar concept in a presentation by John Notte of Zeiss [28] and in a patent application [29].

2) *Continuous-Time Lambert Quotient Mode Estimator*: The CTTR measurement observes a thinned version of the underlying ion incidence process, so $\tilde{M} \leq M$. We can do better than to use \tilde{M} as a proxy for M . Since

$$\mathbb{E}[\tilde{M} | M] = (1 - e^{-\eta})M,$$

$(1 - e^{-\eta})^{-1}\tilde{M}$ would be an unbiased proxy for M . Unfortunately, this has dependence on η , which is not known. In the spirit of the oracle and CTQM estimators, we may seek an estimate $\hat{\eta}$ that satisfies

$$\hat{\eta} = \frac{Y}{(1 - e^{-\hat{\eta}})^{-1}\tilde{M}}.$$

The solution of this equation gives the *continuous-time Lambert quotient mode* (CTLQM) estimator:

$$\hat{\eta}_{\text{CTLQM}} = W(-\hat{\eta}_{\text{CTQM}} e^{-\hat{\eta}_{\text{CTQM}}}) + \hat{\eta}_{\text{CTQM}}, \quad (29)$$

where $W(\cdot)$ is the Lambert W function [30].

3) *Continuous-Time Maximum Likelihood Estimator*: Rather than use a heuristic approximation for the number of incident ions M , one could instead use the statistically principled ML estimation approach as follows. The ML estimate is the value of η that maximizes the joint likelihood of the full CTTR observation.

We have already seen that we can drop the times $\{\tilde{T}_1, \tilde{T}_2, \dots, \tilde{T}_M\}$, and the conditional likelihood of $\{\tilde{X}_1, \tilde{X}_2, \dots, \tilde{X}_M\}$ given \tilde{M} was given in (27). Thus, we must maximize the product of (21) and (27) over η . For observation $(\tilde{M}, \tilde{X}_1, \tilde{X}_2, \dots, \tilde{X}_M) = (\tilde{m}, j_1, j_2, \dots, j_{\tilde{m}})$,

by dropping factors that do not depend on η , we obtain *continuous-time ML* (CTML) estimator

$$\hat{\eta}_{\text{CTML}} = \arg \max_{\eta} e^{-\lambda(1-e^{-\eta})} e^{-\tilde{m}\eta} \eta^y,$$

where $y = j_1 + j_2 + \dots + j_{\tilde{m}}$. The unique maximizer satisfies

$$\hat{\eta}_{\text{CTML}} = \frac{Y}{\tilde{M} + \lambda e^{-\hat{\eta}_{\text{CTML}}}}, \quad (30)$$

which can be solved by using an appropriate root-finding algorithm.

D. Analyzing the Continuous-Time Quotient Mode Estimator

By computing the MSE of $\hat{\eta}_{\text{CTQM}}$, we can evaluate the efficacy of the quotient mode estimator. We begin by noting that

$$\text{MSE}(\hat{\eta}_{\text{CTQM}}) = \text{bias}(\hat{\eta}_{\text{CTQM}})^2 + \text{var}(\hat{\eta}_{\text{CTQM}}). \quad (31)$$

As detailed in Appendix C, the bias is given by

$$\begin{aligned} \text{bias}(\hat{\eta}_{\text{CTQM}}) &= \text{E}[\hat{\eta}_{\text{CTQM}}] - \eta \\ &= \left(\frac{e^{-\eta} - e^{-\lambda(1-e^{-\eta})}}{1 - e^{-\eta}} \right) \eta. \end{aligned} \quad (32)$$

For fixed η , this is a nonzero bias even as dose $\lambda \rightarrow \infty$, consistent with the motivation for defining the CTLQM estimator to improve upon the CTQM estimator. If $\eta \rightarrow \infty$ as well, the bias vanishes, which is consistent with the convergence in distribution of \tilde{M} to M .

As also detailed in Appendix C, the variance is given by

$$\begin{aligned} \text{var}(\hat{\eta}_{\text{CTQM}}) &= \frac{\eta^2}{\rho^2} e^{-\lambda\rho} (1 - e^{-\lambda\rho}) \\ &+ \frac{\eta(\rho - \eta e^{-\eta})}{\rho^2} \sum_{j=1}^{\infty} \frac{1}{j} \frac{e^{-\lambda\rho} (\lambda\rho)^j}{j!}, \end{aligned} \quad (33)$$

where we introduce

$$\rho = \text{P}(X_i > 0) = 1 - e^{-\eta}$$

as a shorthand to make certain expressions more compact. Expression (33) can be combined with (60) from Appendix A to show that the variance vanishes as $\lambda \rightarrow \infty$, decaying asymptotically as $\sim 1/\lambda$. However, because of nonzero bias, the MSE is not inversely proportion to λ , and the MSE of $\hat{\eta}_{\text{CTQM}}$ relative to other estimates depends on λ . Substituting (32) and (33) into (31) gives an expression for the MSE of the CTQM estimator:

$$\begin{aligned} \text{MSE}(\hat{\eta}_{\text{CTQM}}) &= \frac{\eta^2}{\rho^2} (e^{-\eta} - e^{-\lambda\rho})^2 + \frac{\eta^2}{\rho^2} e^{-\lambda\rho} (1 - e^{-\lambda\rho}) \\ &+ \frac{\eta(\rho - \eta e^{-\eta})}{\rho^2} \sum_{j=1}^{\infty} \frac{1}{j} \frac{e^{-\lambda\rho} (\lambda\rho)^j}{j!}. \end{aligned} \quad (34)$$

Substituting the upper bound (61) from Appendix A for the series in (34) gives

$$\begin{aligned} \text{MSE}(\hat{\eta}_{\text{CTQM}}) &< \frac{\eta^2}{\rho^2} (e^{-\eta} - e^{-\lambda\rho})^2 + \frac{\eta^2}{\rho^2} e^{-\lambda\rho} (1 - e^{-\lambda\rho}) \\ &+ 0.518 \frac{\eta(\rho - \eta e^{-\eta})}{\rho^2}. \end{aligned} \quad (35)$$

E. Numerical Comparisons of Estimators

To demonstrate the benefits afforded by CTTR measurement, in Fig. 3 we compare the conventional, oracle, CTQM, CTLQM and CTML estimators across ground truth $\eta \in [0, 10]$. The MSE values in Fig. 3(a) are computed from 150 000 independent Monte Carlo trials, using a dose rate $\Lambda = 1/1600$ ions per ns and dwell time $t = 32 000$ ns, for a total dose $\lambda = 20$ ions per pixel. The curve for $\hat{\eta}_{\text{baseline}}$ matches the theoretical MSE expression (15). Although unimplementable, the curve for $\hat{\eta}_{\text{oracle}}$ also matches the theoretical MSE in (9).¹ We can observe that $\hat{\eta}_{\text{CTQM}}$ has a large MSE for small η , caused largely by \tilde{M} severely underestimating M in these cases. Predictably, $\hat{\eta}_{\text{CTLQM}}$ reduces MSE tremendously for small values of η because the role of \tilde{M} is modified the most in these cases. For low η (about 0 to 2.5), $\hat{\eta}_{\text{CTML}}$ achieves lowest MSE amongst all implementable estimators; for moderate η (about 2.5 to 5.5), $\hat{\eta}_{\text{CTQM}}$ is slightly better than the others; and for large η (about 5.5 and above), $\hat{\eta}_{\text{CTQM}}$, $\hat{\eta}_{\text{CTLQM}}$ and $\hat{\eta}_{\text{CTML}}$ all give nearly identical performance. It is noteworthy that CTQM converges with the oracle at η above about 3.0, though the oracle is unimplementable in practice.

The MSE trends and comparisons can be better understood through the biases in Fig. 3(b) and variances in Fig. 3(c). Curves for $\hat{\eta}_{\text{CTQM}}$ coincide with the bias and variance expressions derived in (32) and (33). As previously noted, the large bias of $\hat{\eta}_{\text{CTQM}}$ for small values of η is caused by the number of incident ions M being severely underestimated by \tilde{M} . The bias of $\hat{\eta}_{\text{CTQM}}$ can be corrected by the use of $\hat{\eta}_{\text{CTLQM}}$. The dashed cyan-colored curve in Fig. 3(c) is the CRB for any unbiased estimator, which is the reciprocal of (26). The variances of the implementable and approximately unbiased $\hat{\eta}_{\text{CTLQM}}$ and $\hat{\eta}_{\text{CTML}}$ estimators approximately coincide with the CRB.

IV. DISCRETE-TIME TIME-RESOLVED MEASUREMENT

A. Measurement Distributions

The DTTR measurement (7) is a length- n vector of SE counts collected over subacquisition dwell times of t/n . Thus, some modeling and analysis for DTTR measurement follows from scaling of λ in expressions from Section II-D. Since $\{Y_1, Y_2, \dots, Y_n\}$ are independent, their joint PMF is simply

$$\text{P}_{Y_1, Y_2, \dots, Y_n}(y_1, y_2, \dots, y_n; \eta, \lambda) = \prod_{k=1}^n \text{P}_Y(y_k; \eta, \lambda/n), \quad (36)$$

written in terms of the PMF in (11).

B. Fisher Information

To evaluate the FI about η in the DTTR measurement (7) with λ as a known parameter is also quite simple. Because FI is additive over independent observations,

$$\mathcal{I}_{\text{DTTR}}(\eta; \lambda, n) = n \mathcal{I}_Y(\eta; \lambda/n), \quad (37)$$

expressed in terms of the FI in (17). While this FI inherits the complexity and lack of interpretability of (17), the distinction

¹We did not need to choose a value for η_0 because the event $\{M = 0\}$, which has probability $e^{-20} \approx 2 \cdot 10^{-9}$, did not occur in any of the trials.

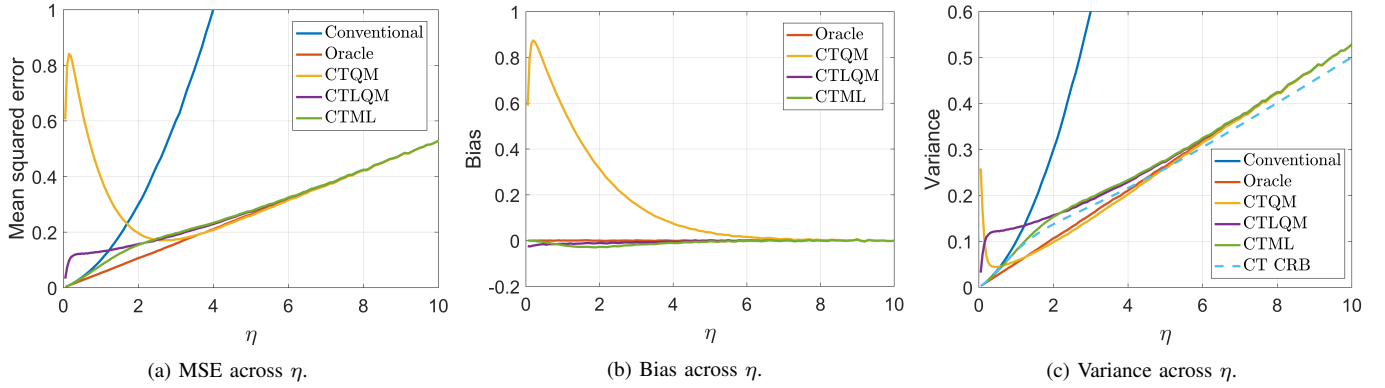


Fig. 3: Comparison of continuous-time time-resolved measurement estimators as a function of η . Conventional, oracle, continuous-time quotient mode, continuous-time Lambert quotient mode, and continuous-time maximum likelihood estimators are simulated for dose rate $\Lambda = 1/1600$ ions per ns and dwell time $t = 32000$ ns, hence total dose $\lambda = 20$ ions per pixel. (a) MSE. (b) Bias. (Conventional estimator omitted because its bias is zero.) (c) Variance.

is that the relevant dose parameter in \mathcal{I}_Y has been reduced from λ to λ/n , so it is more reasonable to approximate with the low-dose asymptote (18). Specifically, we can write

$$\begin{aligned} \mathcal{I}_{\text{DTTR}}(\eta; \lambda, n) &= \lambda \frac{\mathcal{I}_Y(\eta; \lambda/n)}{\lambda/n} \\ &\approx \lambda \left(\frac{1}{\eta} - e^{-\eta} \right), \end{aligned} \quad (38)$$

where the approximation holds for large enough n because of (18). Note that (38) has the same expression as (26), so as $n \rightarrow \infty$, the FI of DTTR measurement converges from below to the FI of CTTR measurement.

C. Estimators

In this section, we present estimators applicable to DTTR measurement (7) that were first introduced in [19]. The subsequent analyses are new.

1) *Discrete-Time Quotient Mode Estimator*: Similar to the principle behind the CTQM estimator (28), the number of subacquisitions with positive SEs,

$$L = \sum_{k=1}^n \mathbb{1}_{\{Y_k > 0\}}, \quad (39)$$

can be a proxy for the number of incident ions M . The *discrete-time quotient mode* (DTQM) estimator is then defined as

$$\hat{\eta}_{\text{DTQM}}(L, Y) = \begin{cases} 0, & L = 0; \\ Y/L, & L > 0. \end{cases} \quad (40)$$

2) *Discrete-Time Lambert Quotient Mode Estimator*: At low η , M is severely underestimated by L . Correspondingly, the *discrete-time Lambert quotient mode* (DTLQM) estimator is obtained by incorporating the correction factor $(1 - e^{-\eta})^{-1}$,

$$\hat{\eta} = \frac{Y}{(1 - e^{-\hat{\eta}})^{-1} L}.$$

The solution of this equation gives the estimator:

$$\hat{\eta}_{\text{DTLQM}} = W(-\hat{\eta}_{\text{DTQM}} e^{-\hat{\eta}_{\text{DTQM}}}) + \hat{\eta}_{\text{DTQM}}. \quad (41)$$

3) *Discrete-Time Maximum Likelihood Estimator*: The *discrete-time ML* (DTML) estimate is the value of η that maximizes the joint likelihood in (36):

$$\hat{\eta}_{\text{DTML}} = \arg \max_{\eta} \prod_{k=1}^n P_Y(y_k; \eta, \lambda/n), \quad (42)$$

where $P_Y(\cdot; \cdot, \cdot)$ is given by (11). Unlike in the CTTR case, we have no fixed-point form for the estimator. Instead, it can be computed by direct numerical optimization. Since the decision variable is scalar, even a simple grid search is not impractical.

D. Analyzing the Discrete-Time Quotient Mode Estimator

Like in Section III-D, we analyze the MSE of $\hat{\eta}_{\text{DTQM}}$ by finding expressions for its bias and variance. In both calculations, we make use of a zero-truncated modification of the Neyman Type A distribution at ion incidence parameter λ/n . Let $p = P(Y_k > 0)$. Then using (11), we find

$$p = 1 - P_Y(0; \eta, \lambda/n) = 1 - \exp\left(-\frac{\lambda}{n}(1 - e^{-\eta})\right). \quad (43)$$

If \tilde{Y}_k is the zero-truncated version of Y_k , then its PMF is

$$P_{\tilde{Y}_k}(y_k) = \frac{1}{p} \frac{e^{-\lambda/n} \eta^{y_k}}{y_k!} \sum_{m=0}^{\infty} \frac{(\lambda/n e^{-\eta})^m m^{y_k}}{m!}, \quad y_k = 1, 2, \dots, \quad (44)$$

its mean is

$$E[\tilde{Y}_k] = \frac{1}{p} \frac{\lambda \eta}{n}, \quad (45)$$

and its variance is

$$\text{var}(\tilde{Y}_k) = \frac{1}{p} \left(\frac{\lambda}{n} \eta + \frac{\lambda}{n} \eta^2 + \left(\frac{\lambda}{n} \eta \right)^2 \right) - \frac{1}{p^2} \left(\frac{\lambda}{n} \eta \right)^2. \quad (46)$$

Furthermore, as a sum of independent indicator random variables, L is a binomial random variable with n trials and success probability p for each trial.

For $\ell > 0$,

$$\begin{aligned} \mathbb{E}[\hat{\eta}_{\text{DTQM}} | L = \ell] &= \mathbb{E}\left[\frac{Y}{L} | L = \ell\right] = \frac{1}{\ell} \mathbb{E}[Y | L = \ell] \\ &\stackrel{(a)}{=} \frac{1}{\ell} \mathbb{E}\left[\sum_{j=1}^{\ell} \tilde{Y}_j\right] = \mathbb{E}[\tilde{Y}_k], \end{aligned} \quad (47)$$

where (a) follows from using \tilde{Y}_j to denote the j th positive subacquisition Y_k . Trivially,

$$\mathbb{E}[\hat{\eta}_{\text{DTQM}} | L = 0] = 0. \quad (48)$$

Using $\mathbb{P}(L > 0) = 1 - (1 - p)^n$ and the total expectation theorem to combine (47) and (48) gives

$$\mathbb{E}[\hat{\eta}_{\text{DTQM}}] = \mathbb{E}[\tilde{Y}_k](1 - (1 - p)^n).$$

The bias of $\hat{\eta}_{\text{DTQM}}$ is thus given by

$$\begin{aligned} \text{bias}(\hat{\eta}_{\text{DTQM}}) &= \mathbb{E}[\hat{\eta}_{\text{DTQM}}] - \eta \\ &= \frac{\lambda\eta}{np} [1 - (1 - p)^n] - \eta, \end{aligned} \quad (49)$$

where (45) has been substituted.

Similar arguments, detailed in Appendix D, yield

$$\begin{aligned} \text{var}(\hat{\eta}_{\text{DTQM}}) &= \left(\mathbb{E}[\tilde{Y}_k]\right)^2 [1 - (1 - p)^n] (1 - p)^n \\ &\quad + \text{var}(\tilde{Y}_k) \sum_{\ell=1}^n \frac{1}{\ell} \binom{n}{\ell} p^\ell (1 - p)^{n-\ell}, \end{aligned} \quad (50)$$

where $\mathbb{E}[\tilde{Y}_k]$ is given in (45) and $\text{var}(\tilde{Y}_k)$ is given in (46). Since the behavior of the series in (50) for large n is not evident, we also derive in Appendix D the lower bound

$$\begin{aligned} \text{var}(\hat{\eta}_{\text{DTQM}}) &\geq \left(\mathbb{E}[\tilde{Y}_k]\right)^2 [1 - (1 - p)^n] (1 - p)^n \\ &\quad + \text{var}(\tilde{Y}_k) \frac{[1 - (1 - p)^n]^2}{np}. \end{aligned} \quad (51)$$

The expressions in (50) and (51) can be added to the square of the bias from (49) to obtain the MSE of $\hat{\eta}_{\text{DTQM}}$ and a lower bound for this MSE.

High n Limits: One of the themes of this paper is that the CTTR measurement model is easier to analyze than the DTTR measurement model, yet it gives expressions relevant to understanding the practical DTTR measurement setting. We would like to examine properties of $\hat{\eta}_{\text{DTQM}}$ at the high n limit, in part to demonstrate that we obtain matches to $\hat{\eta}_{\text{CTQM}}$ behavior.

For the limit of the bias, we will use two facts proven in Appendix E:

$$\lim_{n \rightarrow \infty} np = \lambda(1 - e^{-\eta}), \quad (52)$$

$$\lim_{n \rightarrow \infty} (1 - p)^n = e^{-\lambda(1 - e^{-\eta})}. \quad (53)$$

By substituting (52) and (53) into (49),

$$\begin{aligned} \lim_{n \rightarrow \infty} \text{bias}(\hat{\eta}_{\text{DTQM}}) &= \frac{\lambda\eta}{\lambda(1 - e^{-\eta})} (1 - e^{-\lambda(1 - e^{-\eta})}) - \eta \\ &= \left(\frac{e^{-\eta} - e^{-\lambda(1 - e^{-\eta})}}{1 - e^{-\eta}}\right) \eta, \end{aligned} \quad (54)$$

an exact match to $\text{bias}(\hat{\eta}_{\text{CTQM}})$ in (32).

For the limit of the variance, we will use two additional facts proven in Appendix E:

$$\lim_{n \rightarrow \infty} \mathbb{E}[\tilde{Y}_k] = \frac{\eta}{1 - e^{-\eta}}, \quad (55)$$

$$\lim_{n \rightarrow \infty} \text{var}(\tilde{Y}_k) = \frac{\eta - (\eta + \eta^2)e^{-\eta}}{(1 - e^{-\eta})^2}. \quad (56)$$

Along with substitution of limits, we recognize that the summand in (50) includes a binomial probability for which there is a Poisson limit because np approaches a positive constant [31]:

$$\binom{n}{\ell} p^\ell (1 - p)^{n-\ell} \rightarrow \frac{(\lambda(1 - e^{-\eta}))^\ell}{\ell!} e^{-\lambda(1 - e^{-\eta})}. \quad (57)$$

It is now tedious but straightforward to substitute (52), (53), (55), (56), and (57) into (50) to obtain

$$\lim_{n \rightarrow \infty} \text{var}(\hat{\eta}_{\text{DTQM}}) = \text{var}(\hat{\eta}_{\text{CTQM}}), \quad (58)$$

where $\text{var}(\hat{\eta}_{\text{CTQM}})$ is given in (33).

E. Numerical Comparisons of Estimators

Fig. 4 shows the MSE, bias, and variance of $\hat{\eta}_{\text{DTQM}}$ as functions of the number of subacquisitions n when $\lambda = 10$ and $\eta = 5$. Fig. 4(b) shows the bias approaching the asymptote given by (54). Fig. 4(a) and Fig. 4(c) show the MSE and variance and their lower bounds based on (51). When n is sufficiently large, these are small and close to the Cramér–Rao bound.

Fig. 5 compares the conventional, oracle, DTQM, DTLQM, and DTML estimators across ground truth $\eta \in [0, 10]$. MSE, bias, and variance are computed by Monte Carlo simulation using total dose $\lambda = 20$ split over $n = 200$ subacquisitions. The conventional curves match those in the CT setting in Fig. 3. The DTQM estimator has a large bias for smaller η , which is absent from the DTLQM estimator. Unlike in CT, where the bias for all the studied estimators vanish at moderate and high η , both the DTQM and DTLQM estimator have substantial bias that is approximately linear in η for moderate and high η . The lack of bias of the DTML estimator explains its uniform superiority over the DTQM and DTLQM estimators; this contrasts with the CT setting in which CTQM, CTLQM, and CTML estimators have nearly equal MSE at moderate and high η .

V. SIMULATED MICROSCOPY RESULTS

Figures 3 and 5 show that time-resolved estimators improve upon the conventional processing of abstracted FIB microscope data, and Fig. 4 shows that the performances of DTTR estimators improve with increasing numbers of subacquisitions, converging to the performances of corresponding CTTR estimators. We conclude with visual results to demonstrate these properties in simulated FIB microscopy experiments.

We use the *Hairstyle*² image from ThermoFisher Scientific (upper-left of Fig 6) as the ground truth image, scaled to

²A SEM image of the upper part of the style and stigma from an Arabidopsis flower, https://www.flickr.com/photos/fei_company/9316514268/in/set-72157634429801580/

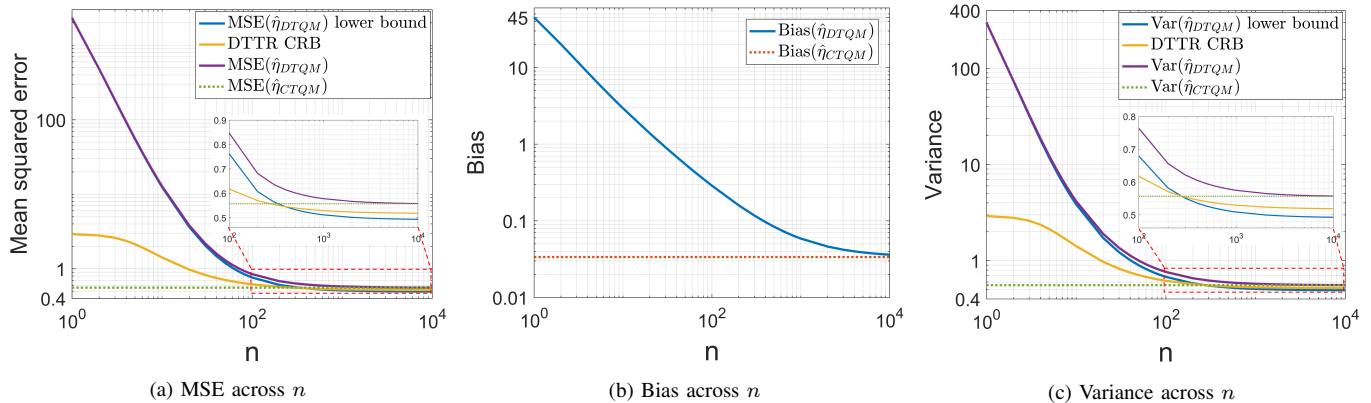


Fig. 4: MSE, bias, and variance of $\hat{\eta}_{\text{DTQM}}$ as functions of the number of subacquisitions n and those of $\hat{\eta}_{\text{CTQM}}$ (dashed lines) for $\lambda = 10$ and $\eta = 5$. The Cramér–Rao lower bound for time-resolved measurements (yellow, see (37)) is plotted as well.

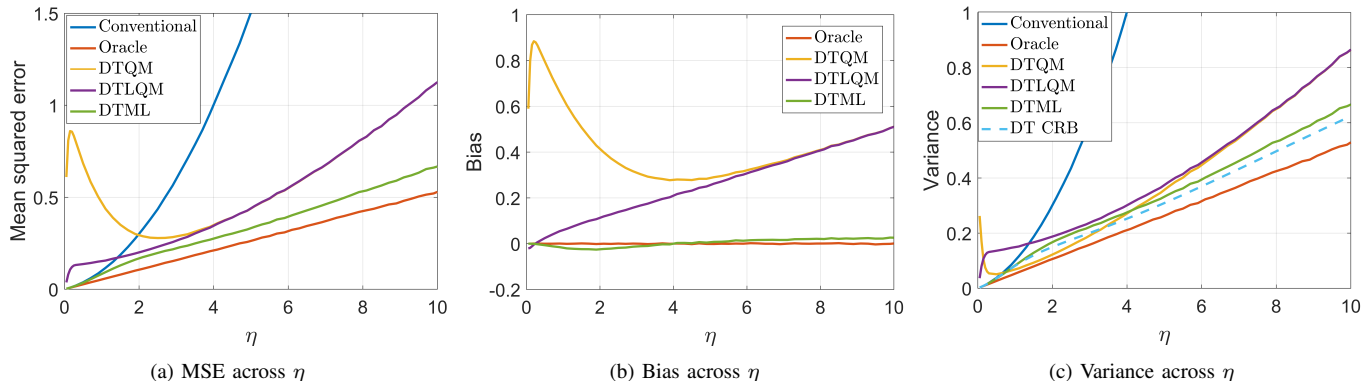


Fig. 5: Comparison of discrete-time time-resolved estimators as a function of η . Conventional, oracle, discrete-time quotient mode, discrete-time Lambert quotient mode, and discrete-time maximum likelihood estimators are simulated for total dose $\lambda = 20$ split over $n = 200$ subacquisitions. (a) MSE. (b) Bias. (Conventional estimator excluded because its bias is zero.) (c) Variance.

have SE yield $\eta \in [1, 8]$. All experiments use total dose $\lambda = 20$. Fig. 6 displays absolute error images for quotient mode, Lambert quotient mode and maximum likelihood estimators. CTTR measurements are simulated and, by division of the dwell time, also interpreted as DTTR measurements for $n \in \{50, 100, 200, 500\}$ subacquisitions. Fig. 7 complements Fig. 6 by plotting MSEs as functions of n for these and additional values of n .

In Fig. 6, each estimator shows improving performance as n increases, with $n = 500$ coming close to the CT performance. With n increased to 2000 in Fig. 7, convergence to CT performance is more clearly indicated. For each value of n , the ranking of estimators has ML best, LQM second, and QM worst. For $n \geq 100$, all the TR methods perform better than the conventional estimator. One way to summarize is to see that with a factor of 4.4 separating the MSEs of the conventional and oracle estimators, the CTML estimator achieves a 3.6 times lower MSE than the conventional estimator.

VI. CONCLUSION

In this work, we establish an abstract framework for TR measurement in FIB microscopy with direct electron detection. Through estimation-theoretic analyses, analyses of estimators, and Monte Carlo FIB imaging simulations, we show the extent to which source shot noise can be mitigated by TR

measurement methods. The most easily interpreted conclusion comes from the Fisher information of continuous-time TR measurements $\lambda(1/\eta - e^{-\eta})$ in (26); when η is not too small, this is only slightly smaller than the λ/η , which is equal to the FI that would be obtained with a deterministic incident particle beam. The dependence on mean SE yield η shows that TR methods have greater TR potential in FIB microscopy than in SEM.

Continuous-time measurement is not implementable in any foreseeable technology. Instead, it is intended as a greatly simpler way to understand the limits of performance under very fine time resolution than to consider $n \rightarrow \infty$ limits for discrete-time results. Through performance comparisons such as those in Figs. 4, 6, and 7, one can predict the time resolution that is necessary to approach the CT limit within a desired margin. Necessary time resolution can also be understood through the use of Fig. 2 to choose a sufficiently small value for λ/n . For example, for the illustrated value of $\eta = 3$, the normalized Fisher information plot suggests that when the time resolution is fine enough for $\lambda/n < 0.1$, at least 83% of the improvement created by time-resolved measurement will be attained.

We study three types of unconventional estimators for both continuous- and discrete-time TR measurements. QM estimators are the simplest to implement and are similar to estimators

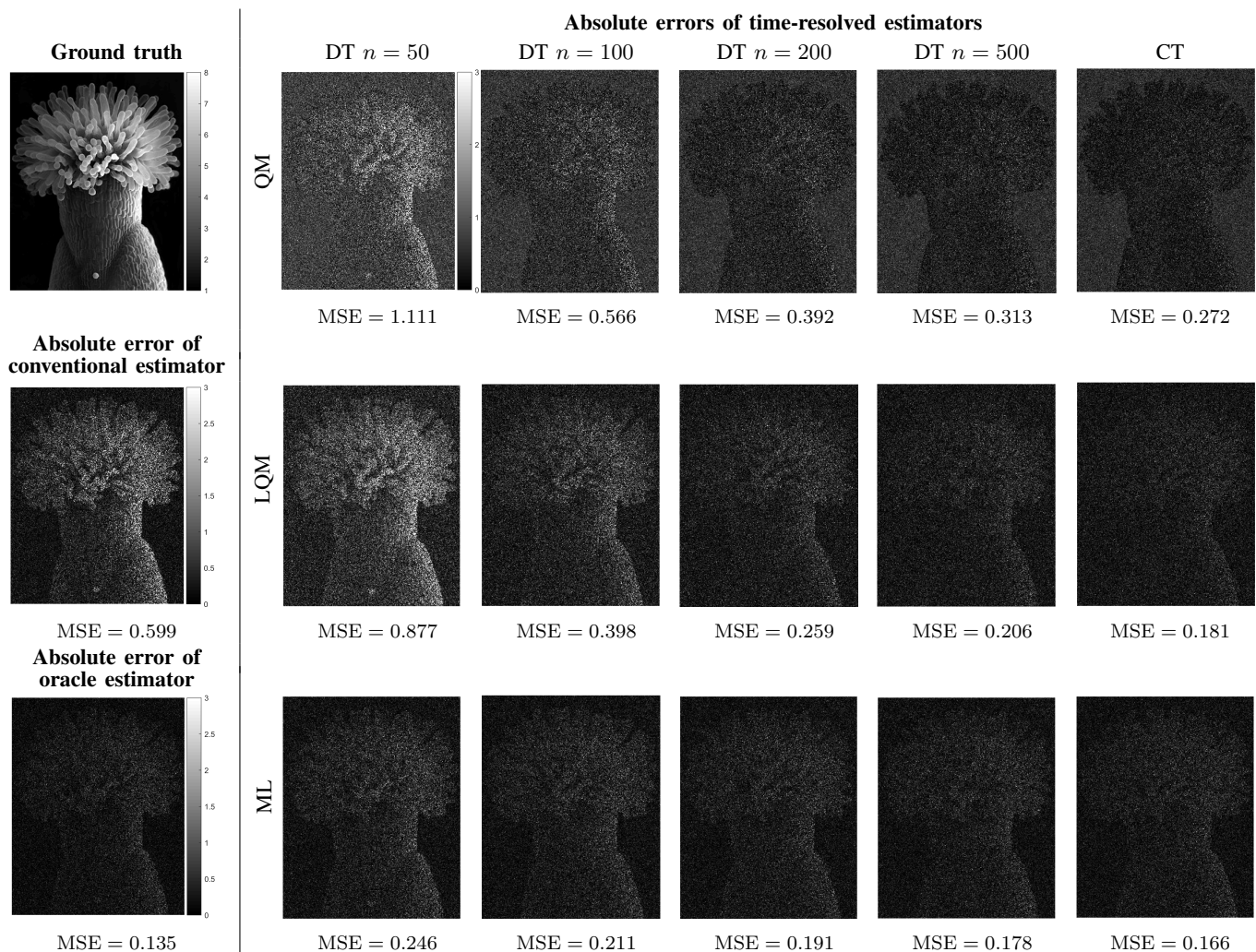


Fig. 6: Simulated FIB microscopy experiment with time-resolved estimators under discrete- and continuous-time settings. Aside from the ground truth in the upper-left corner, with $\eta \in [1, 8]$, all images are of the absolute value of the error. All results are for total dose $\lambda = 20$ mean incident ions per pixel. The columns of time-resolved estimators are for increasing numbers of subacquisitions n , culminating in the limiting continuous-time case. Quotient mode, Lambert quotient mode, maximum likelihood estimators are compared, with the conventional estimator (14) and oracle estimator (8) provided for context. None of these estimators include spatial regularization.

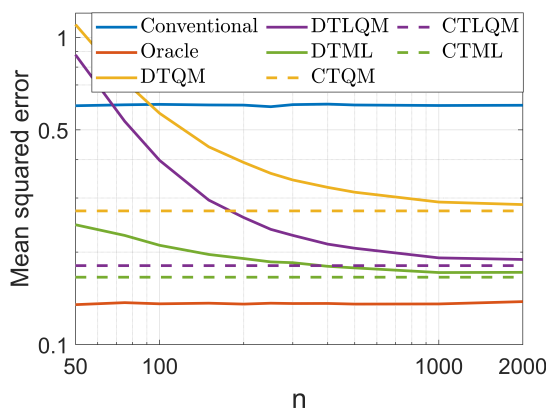


Fig. 7: Mean-squared errors as functions of number of subacquisitions n in simulated FIB microscopy of the image in Fig. 6 using conventional, oracle, quotient mode, Lambert quotient mode, and maximum-likelihood estimators. Total dose is $\lambda = 20$, and mean secondary yield η of the ground truth image is scaled to $[1, 8]$.

proposed by Zeiss but not made commercially available. LQM estimators greatly reduce a source of bias at low η and merely require a table lookup to be applied to QM estimates. ML estimators require root-finding or minimization of a non-convex function. The relationships among the estimators are nontrivial: though generally best, the ML estimator does not outperform the others uniformly over η ; and though far better at low η , the LQM estimator does not outperform the QM estimator uniformly over η .

The improvements presented here seem to be rooted entirely in making the number of incident ions estimable, and this is potentially applicable even without direct SE detection. Indirect electron detection creates uncertainty in the number of detected SEs, including uncertainty in whether any SEs were detected and hence in whether an ion was incident. However, the experimental results of [19] suggest that the degradation in mitigating source shot noise can be small, since the improvements presented therein are similar to the results presented here. The QM and LQM estimators may be

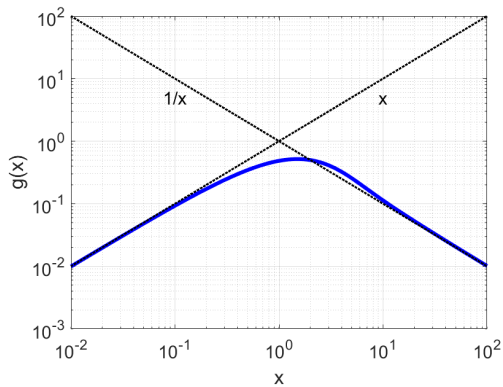


Fig. 8: Function $g(x)$ in (59) along with low- and high- x asymptotes.

extended to cases in which the probabilistic model relating measurements to numbers of SEs is complicated or uncertain. For an advantage from TR measurement, it may be enough to have a mean instrument output that is monotonically increasing with the number of detected SEs. Then a QM or LQM estimator can use \tilde{M} or $(1 - e^{-\eta})^{-1}\tilde{M}$ to normalize a sum of nonlinearly scaled TR measurements to mitigate source shot noise. This is one of several lines of inquiry suggested by the results presented here.

APPENDIX A

HIGH-DOSE PERFORMANCE OF ORACLE ESTIMATOR

Let

$$g(x) = e^{-x} \sum_{m=1}^{\infty} \frac{1}{m} \frac{x^m}{m!}. \quad (59)$$

This function appears in the performance of the oracle estimator (9) and the variance (33) and MSE (34) of the CTQM estimator. We are interested in approximating and bounding $g(x)$ to better understand those expressions.

For $x \ll 1$, the first term is dominant, so $g(x) \approx x$. The behavior at large x is less obvious. The series in (59) converges to $\text{Ei}(x) - \gamma - \log x$, where $\text{Ei}(x)$ is the exponential integral function and γ is the Euler–Mascheroni constant [32]. Asymptotically for $x \rightarrow \infty$, $\text{Ei}(x) \sim e^x/x$, meaning that the ratio of the expressions approaches 1. Thus,

$$g(x) \sim \frac{1}{x}. \quad (60)$$

The log-log plot of $g(x)$ in Fig. 8 shows the accuracies of the low- and high- x approximations. Being nonnegative, continuous, and vanishing as $x \rightarrow \infty$, $g(x)$ has a finite upper bound:

$$g(x) \leq 0.518, \quad \text{for all } x \in [0, \infty). \quad (61)$$

APPENDIX B

NORMALIZED FISHER INFORMATION LIMITS

A. Low-Dose Limit

To evaluate $\lim_{\lambda \rightarrow 0} \mathcal{I}_Y(\eta; \lambda)/\lambda$, we first find $\lambda \rightarrow 0$ limits of expressions that appear in (17), including both the PMF in (11) and the probability ratio $P_Y(y+1; \eta, \lambda)/P_Y(y; \eta, \lambda)$.

For $y = 0$,

$$P_Y(0; \eta, \lambda) = \frac{e^{-\lambda}\eta^0}{0!} \sum_{m=0}^{\infty} \frac{(\lambda e^{-\eta})^m m^0}{m!} \\ \stackrel{(a)}{=} e^{-\lambda} \sum_{m=0}^{\infty} \frac{(\lambda e^{-\eta})^m}{m!} \stackrel{(b)}{=} e^{-\lambda} \exp(\lambda e^{-\eta}), \quad (62)$$

where (a) follows from $m^0 = 1$; and (b) from identifying the series expansion of the exponential function. Similarly, for $y = 1$,

$$P_Y(1; \eta, \lambda) = \frac{e^{-\lambda}\eta^1}{1!} \sum_{m=0}^{\infty} \frac{(\lambda e^{-\eta})^m m^1}{m!} \\ = (e^{-\lambda}\eta)(\lambda e^{-\eta}) \exp(\lambda e^{-\eta}), \quad (63)$$

and for $y = 2$,

$$P_Y(2; \eta, \lambda) = \frac{e^{-\lambda}\eta^2}{2!} \sum_{m=0}^{\infty} \frac{(\lambda e^{-\eta})^m m^2}{m!} \\ = \frac{e^{-\lambda}\eta^2}{2} (\lambda e^{-\eta})(1 + \lambda e^{-\eta}) \exp(\lambda e^{-\eta}). \quad (64)$$

For general $y > 0$,

$$P_Y(y; \eta, \lambda) = \frac{e^{-\lambda}\eta^y}{y!} \sum_{m=0}^{\infty} \frac{(\lambda e^{-\eta})^m m^y}{m!} \\ = \frac{e^{-\lambda}\eta^y}{y!} (\lambda e^{-\eta}) \text{poly}_{y-1}(\lambda e^{-\eta}) \exp(\lambda e^{-\eta}), \quad (65)$$

where $\text{poly}_y(\lambda e^{-\eta})$ is a degree- y polynomial in $\lambda e^{-\eta}$ with unit constant term. This allows us to conclude, for any $y > 0$,

$$\lim_{\lambda \rightarrow 0} \frac{P_Y(y; \eta, \lambda)}{\lambda} = \frac{\eta^y}{y!} e^{-\eta}. \quad (66)$$

From (62) and (63), we obtain, for $y = 0$,

$$\frac{P_Y(y+1; \eta, \lambda)}{P_Y(y; \eta, \lambda)} = \frac{P_Y(1; \eta, \lambda)}{P_Y(0; \eta, \lambda)} = \eta \lambda e^{-\eta}. \quad (67)$$

From (63) and (64), we obtain, for $y = 1$,

$$\frac{P_Y(y+1; \eta, \lambda)}{P_Y(y; \eta, \lambda)} = \frac{P_Y(2; \eta, \lambda)}{P_Y(1; \eta, \lambda)} = \frac{1}{2} \eta (1 + \lambda e^{-\eta}). \quad (68)$$

For general $y > 0$, it follows from (66) that

$$\lim_{\lambda \rightarrow 0} \frac{P_Y(y+1; \eta, \lambda)}{P_Y(y; \eta, \lambda)} = \frac{\eta}{y+1}. \quad (69)$$

Now to evaluate $\lim_{\lambda \rightarrow 0} \mathcal{I}_Y(\eta; \lambda)/\lambda$, we can pass the limit through to each term in (17). The first term is

$$\lim_{\lambda \rightarrow 0} \left(\frac{0}{\eta} - \frac{P_Y(1; \eta, \lambda)}{P_Y(0; \eta, \lambda)} \frac{1}{\eta} \right)^2 \frac{P_Y(0; \eta, \lambda)}{\lambda} \\ \stackrel{(a)}{=} \lim_{\lambda \rightarrow 0} \left(\frac{0}{\eta} - \eta \lambda e^{-\eta} \frac{1}{\eta} \right)^2 \frac{e^{-\lambda} \exp(\lambda e^{-\eta})}{\lambda} = 0,$$

where (a) follows from (62) and (67). By substituting (66) and (69) in (17), the remaining terms give

$$\lim_{\lambda \rightarrow 0} \frac{\mathcal{I}_Y(\eta; \lambda)}{\lambda} = \sum_{y=1}^{\infty} \left(\frac{y}{\eta} - \frac{\eta}{y+1} \frac{y+1}{\eta} \right)^2 \frac{\eta^y}{y!} e^{-\eta} \\ = \sum_{y=1}^{\infty} \left(\frac{y}{\eta} - 1 \right)^2 \frac{\eta^y}{y!} e^{-\eta} = \left(\frac{e^{\eta}}{\eta} - 1 \right) e^{-\eta} = \frac{1}{\eta} - e^{-\eta}.$$

This proves (18), as desired.

B. High-Dose Limit

Let us first compute the Fisher information for the parameter η when a Gaussian random variable has mean η and variance $f(\eta)$ for some twice-differentiable function f . Let $S \sim \mathcal{N}(\eta, f(\eta))$. Then the log-likelihood of S is

$$\log f_S(s; \eta) = -\frac{1}{2} \log(2\pi) - \frac{1}{2} \log f(\eta) - \frac{(s - \eta)^2}{2f(\eta)}. \quad (70)$$

The derivative of $\log f_S(s; \eta)$ with respect to η is

$$\frac{\partial \log f_S(s; \eta)}{\partial \eta} = -\frac{f'(\eta)}{2f(\eta)} - \frac{2(\eta - s)f(\eta) - (\eta - s)^2 f'(\eta)}{2f(\eta)^2}.$$

The second derivative is then

$$\begin{aligned} \frac{\partial^2 \log f_S(s; \eta)}{\partial \eta^2} &= -\frac{f''(\eta)f(\eta) - f'(\eta)^2}{2f(\eta)^2} - \frac{1}{f(\eta)} \\ &\quad + \frac{2f'(\eta)}{f(\eta)^2}(\eta - s) \\ &\quad - \frac{2[f'(\eta)]^2 - f''(\eta)f(\eta)}{2f(\eta)^3}(\eta - s)^2. \end{aligned}$$

The Fisher information for the estimation of η is

$$\begin{aligned} \mathcal{I}_S(\eta) &= \mathbb{E} \left[-\frac{\partial^2 \log f_S(S; \eta)}{\partial \eta^2}; \eta \right] \\ &= \frac{f''(\eta)f(\eta) - f'(\eta)^2}{2f(\eta)^2} + \frac{1}{f(\eta)} - \frac{2f'(\eta)}{f(\eta)^2} \mathbb{E}[\eta - S] \\ &\quad + \frac{2[f'(\eta)]^2 - f''(\eta)f(\eta)}{2f(\eta)^3} \mathbb{E}[(\eta - S)^2] \\ &\stackrel{(a)}{=} \frac{f''(\eta)f(\eta) - f'(\eta)^2}{2f(\eta)^2} + \frac{1}{f(\eta)} - \frac{2f'(\eta)}{f(\eta)^2} \cdot 0 \\ &\quad + \frac{2[f'(\eta)]^2 - f''(\eta)f(\eta)}{2f(\eta)^3} \cdot f(\eta) \\ &= \frac{1}{f(\eta)} + \frac{[f'(\eta)]^2}{2f(\eta)^2}, \end{aligned} \quad (71)$$

where (a) follows from substituting $\mathbb{E}[\eta - S] = 0$ and $\mathbb{E}[(\eta - S)^2] = \text{var}(S) = f(\eta)$. (Note that this simplifies to the familiar reciprocal of the variance when $f(\eta)$ is a constant.)

At high dose, Y/λ is well-approximated as a $\mathcal{N}(\eta, \eta(\eta + 1)/\lambda)$ random variable [33, Sect. IV]. Thus, define $f(\eta) = \eta(\eta + 1)/\lambda$ so that Y/λ is approximated well by S . Substituting $f'(\eta) = (2\eta + 1)/\lambda$ into (71) gives

$$\mathcal{I}_S(\eta) = \frac{\lambda}{\eta(\eta + 1)} + \frac{(2\eta + 1)^2}{2\lambda\eta^2(\eta + 1)^2}. \quad (72)$$

Since $Y \approx \lambda S$,

$$\begin{aligned} \lim_{\lambda \rightarrow \infty} \frac{\mathcal{I}_Y(\eta; \lambda)}{\lambda} &= \lim_{\lambda \rightarrow \infty} \left[\frac{1}{\eta(\eta + 1)} + \frac{(2\eta + 1)^2}{2\lambda\eta^2(\eta + 1)^2} \right] \\ &= \frac{1}{\eta(\eta + 1)}, \end{aligned}$$

as desired.

APPENDIX C

DERIVATION OF MEAN-SQUARED ERROR FOR CONTINUOUS-TIME QUOTIENT MODE ESTIMATOR

A. Bias of $\hat{\eta}_{\text{CTQM}}$

For $m > 0$,

$$\begin{aligned} \mathbb{E} \left[\hat{\eta}_{\text{CTQM}} \mid \tilde{M} = m \right] &= \mathbb{E} \left[\frac{Y}{\tilde{M}} \mid \tilde{M} = m \right] \\ &= \frac{1}{m} \mathbb{E} \left[Y \mid \tilde{M} = m \right] \stackrel{(a)}{=} \frac{1}{m} \mathbb{E} \left[\sum_{i=1}^m \tilde{X}_i \right] = \mathbb{E} \left[\tilde{X}_i \right] \\ &\stackrel{(b)}{=} \frac{\eta}{1 - e^{-\eta}}, \end{aligned} \quad (73)$$

where (a) follows from using (4) as an expression for Y ; and (b) from the effect of zero-truncation on the Poisson(η) distribution. Trivially,

$$\mathbb{E} \left[\hat{\eta}_{\text{CTQM}} \mid \tilde{M} = 0 \right] = 0. \quad (74)$$

Using $\mathbb{P}(\tilde{M} > 0) = 1 - e^{-\lambda(1 - e^{-\eta})}$ from (21) and the total expectation theorem to combine (73) and (74) gives

$$\mathbb{E}[\hat{\eta}_{\text{CTQM}}] = \left(1 - e^{-\lambda(1 - e^{-\eta})}\right) \frac{\eta}{1 - e^{-\eta}}. \quad (75)$$

Subtracting η gives (32).

B. Variance of $\hat{\eta}_{\text{CTQM}}$

From (73) and (74), $\mathbb{E}[\hat{\eta}_{\text{CTQM}} \mid \tilde{M}]$ is a two-valued random variable equal to $\eta/(1 - e^{-\eta})$ with probability $1 - e^{-\lambda(1 - e^{-\eta})}$ and equal to 0 otherwise. Thus,

$$\begin{aligned} \text{var} \left(\mathbb{E} \left[\hat{\eta}_{\text{CTQM}} \mid \tilde{M} \right] \right) &= \frac{\eta^2}{(1 - e^{-\eta})^2} e^{-\lambda(1 - e^{-\eta})} \left(1 - e^{-\lambda(1 - e^{-\eta})}\right) \end{aligned} \quad (76)$$

by direct calculation.

Toward computing $\mathbb{E}[\text{var}(\hat{\eta}_{\text{CTQM}} \mid \tilde{M})]$, let us first examine $\text{var}(\hat{\eta}_{\text{CTQM}} \mid \tilde{M} = m)$. For $m > 0$,

$$\begin{aligned} \text{var} \left(\hat{\eta}_{\text{CTQM}} \mid \tilde{M} = m \right) &= \text{var} \left(\frac{Y}{\tilde{M}} \mid \tilde{M} = m \right) \\ &= \frac{1}{m^2} \text{var} \left(Y \mid \tilde{M} = m \right) \stackrel{(a)}{=} \frac{1}{m^2} \text{var} \left(\sum_{i=1}^m \tilde{X}_i \right) \\ &= \frac{1}{m} \text{var} \left(\tilde{X}_i \right) \stackrel{(b)}{=} \frac{1}{m} \left(\frac{\eta + \eta^2}{1 - e^{-\eta}} - \frac{\eta^2}{(1 - e^{-\eta})^2} \right), \end{aligned} \quad (77)$$

where (a) follows from using (4) as an expression for Y ; and (b) from the effect of zero-truncation on the Poisson(η) distribution. Trivially,

$$\text{var} \left(\hat{\eta}_{\text{CTQM}} \mid \tilde{M} = 0 \right) = 0. \quad (78)$$

Using the PMF of \tilde{M} from (21) and the total expectation theorem to combine (77) and (78) gives

$$\begin{aligned} \mathbb{E} \left[\text{var} \left(\hat{\eta}_{\text{CTQM}} \mid \tilde{M} \right) \right] &= \left(\frac{\eta + \eta^2}{1 - e^{-\eta}} - \frac{\eta^2}{(1 - e^{-\eta})^2} \right) e^{-\lambda(1 - e^{-\eta})} \\ &\quad \cdot \sum_{m=1}^{\infty} \frac{1}{m} \frac{[\lambda(1 - e^{-\eta})]^m}{m!}. \end{aligned} \quad (79)$$

By summing (76) and (79) we obtain the variance of $\hat{\eta}_{\text{CTQM}}$, which verifies (33).

APPENDIX D
DERIVATION OF MEAN-SQUARED ERROR FOR
DISCRETE-TIME QUOTIENT MODE ESTIMATOR

A. Variance of $\hat{\eta}_{\text{DTQM}}$

From (47) and (48), $E[\hat{\eta}_{\text{DTQM}} | L]$ is a two-valued random variable equal to $E[\tilde{Y}_k]$ with probability $1 - (1-p)^n$ and equal to 0 otherwise. Thus,

$$\text{var}(E[\hat{\eta}_{\text{DTQM}} | L]) = \left(E[\tilde{Y}_k]\right)^2 [1 - (1-p)^n](1-p)^n, \quad (80)$$

where $E[\tilde{Y}_k]$ is given in (45).

Toward computing $E[\text{var}(\hat{\eta}_{\text{DTQM}} | L)]$, let us first examine $\text{var}(\hat{\eta}_{\text{DTQM}} | L = \ell)$. For $\ell > 0$,

$$\begin{aligned} \text{var}(\hat{\eta}_{\text{DTQM}} | L = \ell) &= \text{var}\left(\frac{Y}{L} | L = \ell\right) = \frac{1}{\ell^2} \text{var}(Y | L = \ell) \\ &= \frac{1}{\ell^2} \text{var}\left(\sum_{j=1}^{\ell} \tilde{Y}_j\right) = \frac{1}{\ell} \text{var}(\tilde{Y}_k), \end{aligned} \quad (81)$$

where $\text{var}(\tilde{Y}_k)$ is given in (46). Trivially,

$$\text{var}(\hat{\eta}_{\text{DTQM}} | L = 0) = 0. \quad (82)$$

Using the binomial PMF of L and the total expectation theorem to combine (81) and (82) gives

$$E[\text{var}(\hat{\eta}_{\text{DTQM}} | L)] = \text{var}(\tilde{Y}_k) \sum_{\ell=1}^n \frac{1}{\ell} \binom{n}{\ell} p^{\ell} (1-p)^{n-\ell}. \quad (83)$$

By summing (80) and (83) we obtain the variance of $\hat{\eta}_{\text{DTQM}}$, which verifies (50).

B. Variance Lower Bound

Let \tilde{L} be the zero-truncated version of binomial random variable L , with PMF

$$P_{\tilde{L}}(\ell) = \frac{1}{1 - (1-p)^n} \binom{n}{\ell} p^{\ell} (1-p)^{n-\ell}, \quad \ell = 1, 2, \dots, n.$$

Then the series in (50) equals $(1 - (1-p)^n) E[1/\tilde{L}]$. Using Jensen's inequality, we can bound $E[1/\tilde{L}]$ using $E[\tilde{L}]$, which has a simple closed-form expression:

$$E[\tilde{L}] = \frac{1}{1 - (1-p)^n} E[L] = \frac{np}{1 - (1-p)^n}. \quad (84)$$

Specifically,

$$\begin{aligned} \sum_{\ell=1}^n \frac{1}{\ell} \binom{n}{\ell} p^{\ell} (1-p)^{n-\ell} &= (1 - (1-p)^n) E\left[\frac{1}{\tilde{L}}\right] \\ &\stackrel{(a)}{\geq} (1 - (1-p)^n) \frac{1}{E[\tilde{L}]} \stackrel{(b)}{=} \frac{(1 - (1-p)^n)^2}{np}, \end{aligned} \quad (85)$$

where (a) follows from Jensen's inequality; and (b) from (84). Substituting (85) in (50) gives (51).

APPENDIX E
DERIVATION OF HIGH n LIMITS

A. Proof of (52)

$$\begin{aligned} \lim_{n \rightarrow \infty} np &= \lim_{n \rightarrow \infty} \frac{1 - e^{-(\lambda/n)(1-e^{-\eta})}}{1/n} \\ &\stackrel{(a)}{=} \lim_{n \rightarrow \infty} \frac{-e^{-(\lambda/n)(1-e^{-\eta})} (1-e^{-\eta}) \lambda/n^2}{-1/n^2} \\ &= \lim_{n \rightarrow \infty} e^{-(\lambda/n)(1-e^{-\eta})} (1-e^{-\eta}) \lambda \\ &= \lambda(1-e^{-\eta}), \end{aligned}$$

where (a) follows from L'Hôpital's rule.

B. Proof of (53)

$$\begin{aligned} \lim_{n \rightarrow \infty} (1-p)^n &\stackrel{(a)}{=} \lim_{n \rightarrow \infty} \left(\exp\left(-\frac{\lambda}{n}(1-e^{-\eta})\right)\right)^n \\ &= \exp(-\lambda(1-e^{-\eta})) \end{aligned}$$

where (a) follows from substitution of (43).

C. Proof of (55)

$$\begin{aligned} \lim_{n \rightarrow \infty} E[\tilde{Y}_k] &\stackrel{(a)}{=} \lim_{n \rightarrow \infty} \frac{\lambda\eta}{np} \\ &\stackrel{(b)}{=} \lim_{n \rightarrow \infty} \frac{\lambda\eta}{\lambda(1-e^{-\eta})} = \frac{\eta}{1-e^{-\eta}}, \end{aligned}$$

where (a) follows from substitution of (45); and (b) from substitution of (52).

D. Proof of (56)

$$\begin{aligned} \lim_{n \rightarrow \infty} \text{var}(\tilde{Y}_k) &\stackrel{(a)}{=} \lim_{n \rightarrow \infty} \frac{1}{p} \left(\frac{\lambda}{n}\eta + \frac{\lambda}{n}\eta^2 + \left(\frac{\lambda}{n}\eta\right)^2\right) - \frac{1}{p^2} \left(\frac{\lambda}{n}\eta\right)^2 \\ &= \lim_{n \rightarrow \infty} \frac{\lambda\eta}{np} + \frac{\lambda\eta^2}{np} + \frac{\lambda^2\eta^2}{n^2p} - \frac{\lambda^2\eta^2}{n^2p^2} \\ &\stackrel{(b)}{=} \lim_{n \rightarrow \infty} \frac{\lambda\eta + \lambda\eta^2}{\lambda(1-e^{-\eta})} - \frac{\lambda^2\eta^2}{\lambda^2(1-e^{-\eta})^2} \\ &= \frac{\eta - (\eta + \eta^2)e^{-\eta}}{(1-e^{-\eta})^2}, \end{aligned}$$

where (a) follows from substitution of (46); and (b) from substitution of (52) and noting that the third term vanishes.

REFERENCES

- [1] D. McMullan, "Scanning electron microscopy 1928–1965," *Scanning*, vol. 17, no. 3, pp. 175–185, May–Jun. 1995.
- [2] E. W. Müller and T. T. Tsong, *Field Ion Microscopy: Principles and Applications*. American Elsevier, 1969.
- [3] B. W. Ward, J. A. Notte, and N. P. Economou, "Helium ion microscope: A new tool for nanoscale microscopy and metrology," *J. Vacuum Sci. Technol. B*, vol. 24, no. 6, pp. 2871–2874, Nov. 2006.
- [4] D. Emmrich, A. Beyer, A. Nadzeyka, S. Bauerdick, J. Meyer, J. Kotakoski, and A. Götzhäuser, "Nanopore fabrication and characterization by helium ion microscopy," *Appl. Phys. Lett.*, vol. 108, no. 16, p. 163103, 2016.

- [5] M. S. Joens, C. Huynh, J. M. Kasuboski, D. Ferranti, Y. J. Sigal, F. Zeitvogel, M. Obst, C. J. Burkhardt, K. P. Curran, S. H. Chalasani, L. A. Stern, B. Goetze, and J. A. J. Fitzpatrick, "Helium ion microscopy (HIM) for the imaging of biological samples at sub-nanometer resolution," *Sci. Rep.*, vol. 3, no. 3514, 2013.
- [6] S. Bazargan, N. F. Heinig, J. F. Rios, and K. Leung, "Electronic transport in tin (iv) oxide nanocrystalline films: two-medium transport with three-dimensional variable-range hopping mechanism for the ultrasmall nanocrystallite size regime," *J. Physical Chemistry C*, vol. 116, no. 8, pp. 4979–4985, 2012.
- [7] T. Wirtz, O. De Castro, J.-N. Audinot, and P. Philipp, "Imaging and analytics on the helium ion microscope," *Ann. Rev. Analytical Chem.*, vol. 12, pp. 523–543, 2019.
- [8] L. Scipioni, C. A. Sanford, J. Notte, B. Thompson, and S. McVey, "Understanding imaging modes in the helium ion microscope," *J. Vac. Sci. & Technol. B*, vol. 27, no. 6, pp. 3250–3255, 2009.
- [9] R. Ramachandra, B. Griffin, and D. Joy, "A model of secondary electron imaging in the helium ion scanning microscope," *Ultramicroscopy*, vol. 109, no. 6, pp. 748–757, 2009.
- [10] J. Morgan, J. Notte, R. Hill, and B. Ward, "An introduction to the helium ion microscope," *Microscopy Today*, vol. 14, no. 4, pp. 24–31, 2006.
- [11] G. Hlawacek, V. Veligura, R. van Gastel, and B. Poelsema, "Helium ion microscopy," *J. Vac. Sci. & Technol. B*, vol. 32, no. 2, p. 020801, 2014.
- [12] R. Livengood, S. Tan, Y. Greenzweig, J. Notte, and S. McVey, "Sub-surface damage from helium ions as a function of dose, beam energy, and dose rate," *J. Vac. Sci. & Technol. B*, vol. 27, no. 6, pp. 3244–3249, 2009.
- [13] V. Castaldo, C. W. Hagen, P. Kruit, E. Van Veldhoven, and D. Maas, "On the influence of the sputtering in determining the resolution of a scanning ion microscope," *J. Vac. Sci. & Technol. B*, vol. 27, no. 6, pp. 3196–3202, 2009.
- [14] J. Orloff, L. W. Swanson, and M. Utlaut, "Fundamental limits to imaging resolution for focused ion beams," *J. Vac. Sci. & Technol. B*, vol. 14, no. 6, pp. 3759–3763, 1996.
- [15] D. Fox, Y. B. Zhou, A. O'Neill, S. Kumar, J. J. Wang, J. N. Coleman, G. S. Duesberg, J. F. Donegan, and H. Z. Zhang, "Helium ion microscopy of graphene: Beam damage, image quality and edge contrast," *Nanotechnology*, vol. 24, no. 33, p. 335702, 2013.
- [16] H. S. Anderson, J. Ilic-Helms, B. Rohrer, J. Wheeler, and K. Larson, "Sparse imaging for fast electron microscopy," in *SPIE Computational Imaging XI*, vol. 8657, 2013, p. 86570C.
- [17] L. Donati, M. Nilchian, S. Trépout, C. Messaoudi, S. Marco, and M. Unser, "Compressed sensing for STEM tomography," *Ultramicroscopy*, vol. 179, pp. 47–56, 2017.
- [18] F. Boughorbel, P. Potocek, M. Hovorka, L. Strakos, J. Mitchels, T. Vystavel, P. Trampert, B. Lich, and T. Dahmen, "High-throughput large volume sem workflow using sparse scanning and in-painting algorithms inspired by compressive sensing," *Microscopy and Microanalysis*, vol. 23, no. S1, pp. 150–151, 2017.
- [19] M. Peng, J. Murray-Bruce, K. K. Berggren, and V. K. Goyal, "Source shot noise mitigation in focused ion beam microscopy by time-resolved measurement," *Ultramicroscopy*, p. 112948, 2020.
- [20] G. McMullan, S. Chen, R. Henderson, and A. Faruqi, "Detective quantum efficiency of electron area detectors in electron microscopy," *Ultramicroscopy*, vol. 109, no. 9, pp. 1126–1143, 2009.
- [21] S. Yamada, T. Ito, K. Gouhara, and Y. Uchikawa, "Electron-count imaging in SEM," *Scanning*, vol. 13, no. 2, pp. 165–171, 1991.
- [22] L. Jin, A.-C. Milazzo, S. Kleinfelder, S. Li, P. Leblanc, F. Duttweiler, J. C. Bouwer, S. T. Peltier, M. H. Ellisman, and N.-H. Xuong, "Applications of direct detection device in transmission electron microscopy," *J. Structural Biology*, vol. 161, no. 3, pp. 352–358, 2008.
- [23] C. Li, S. F. Mao, and Z. J. Ding, "Time-dependent characteristics of secondary electron emission," *J. Appl. Physics*, vol. 125, no. 024902, Jan. 2019.
- [24] Y. Lin and D. C. Joy, "A new examination of secondary electron yield data," *Surface Interface Anal.*, vol. 37, no. 11, pp. 895–900, 2005.
- [25] J. Notte, B. Ward, N. Economou, R. Hill, R. Percival, L. Farkas, and S. McVey, "An introduction to the helium ion microscope," in *AIP Conference Proceedings*, vol. 931. AIP, 2007, pp. 489–496.
- [26] L. Frank, "Noise in secondary electron emission: the low yield case," *J. Electron Microscopy*, vol. 54, no. 4, pp. 361–365, Aug. 2005.
- [27] H. L. Van Trees, *Detection, Estimation and Modulation Theory, Part I*. New York, NY: Wiley, 2001.
- [28] J. A. Notte, "Imaging with helium ions – A new detector regime with new challenges and new opportunities," American Vacuum Society 60th Int. Symp. Exhibit., Oct. 31 (presented, no proceedings), 2013.
- [29] J. A. Notte, S. Carouso, and B. W. Ward, "Ion beam imaging," World Intellectual Property Organization publication WO 2009/079195 A1, 25 Jun. 2009.
- [30] R. M. Corless, G. H. Gonnet, D. E. G. Hare, D. J. Jeffrey, and D. E. Knuth, "On the Lambert W function," *Advances in Computational Mathematics*, vol. 5, no. 1, pp. 329–359, Dec. 1996.
- [31] R. J. Serfling, "Some elementary results on Poisson approximation in a sequence of Bernoulli trials," *SIAM Rev.*, vol. 20, no. 3, pp. 567–579, Jul. 1978.
- [32] E. Masina, "A review on the exponential-integral special function and other strictly related special functions," arXiv:1907.12373v1 [math.GM], Jul. 2019.
- [33] M. C. Teich, "Role of the doubly stochastic Neyman type-A and Thomas counting distributions in photon detection," *Appl. Optics*, vol. 20, no. 14, pp. 2457–2467, Jul. 1981.